

Magnetic state selected by magnetic dipole interaction in the kagome antiferromagnet NaBa₂Mn₃F₁₁Shohei Hayashida,¹ Hajime Ishikawa,² Yoshihiko Okamoto,³ Tsuyoshi Okubo,⁴ Zenji Hiroi,¹ Maxim Avdeev,^{5,6} Pascal Manuel,⁷ Masato Hagihala,¹ Minoru Soda,¹ and Takatsugu Masuda¹¹*Institute for Solid State Physics, The University of Tokyo, Chiba 277-8581, Japan*²*Institute for Functional Matter and Quantum Technologies, University of Stuttgart, Pfaffenwaldring 57, 70569 Stuttgart, Germany*³*Department of Applied Physics, Nagoya University, Nagoya 464-8603, Japan*⁴*Department of Physics, The University of Tokyo, Tokyo 113-0033, Japan*⁵*Australian Nuclear Science and Technology Organization, Menai, New South Wales 2234, Australia*⁶*School of Chemistry, The University of Sydney, Sydney, New South Wales 2006, Australia*⁷*ISIS Pulsed Neutron and Muon Source, Rutherford Appleton Laboratory, Chilton, Didcot OX11 0QX, United Kingdom*

(Received 11 June 2017; published 12 February 2018)

We have studied the ground state of the classical kagome antiferromagnet NaBa₂Mn₃F₁₁. Strong magnetic Bragg peaks observed for d spacings shorter than 6.0 Å were indexed by the propagation vector of $\mathbf{k}_0 = (0, 0, 0)$. Additional peaks with weak intensities in the d -spacing range above 8.0 Å were indexed by the incommensurate vector of $\mathbf{k}_1 = [0.3209(2), 0.3209(2), 0]$ and $\mathbf{k}_2 = [0.3338(4), 0.3338(4), 0]$. Magnetic structure analysis unveils a 120° structure with the *tail-chase* geometry having \mathbf{k}_0 modulated by the incommensurate vector. A classical calculation of the Heisenberg kagome antiferromagnet with antiferromagnetic second-neighbor interaction, for which the ground state a \mathbf{k}_0 120° degenerated structure, reveals that the magnetic dipole-dipole (MDD) interaction including up to the fourth neighbor terms selects the tail-chase structure. The observed modulation of the tail-chase structure is attributed to a small perturbation such as the long-range MDD interaction or the interlayer interaction.

DOI: [10.1103/PhysRevB.97.054411](https://doi.org/10.1103/PhysRevB.97.054411)**I. INTRODUCTION**

Long-range magnetic dipole-dipole (MDD) interaction is ubiquitous in nature. The texture of iron filings around a bar magnet is a visualization of the MDD interaction which is familiar to schoolchildren, and the anisotropic deformation of condensed magnetic atoms at a low temperature is at the forefront of modern science [1]. In insulating magnets, effective quantum spins having large magnitudes of moments coupled via the MDD interaction give easy access to observations of novel quantum phenomena [2–4]. In artificial mesomagnets the vortex cores dominated by the long-range MDD interaction exhibit complex collective dynamics in magnonic crystals [5–7]. In bulk magnets composed of 3d transition metals, however, the MDD interaction is not necessarily a primary interaction but rather a small liaison to transfer the information of the lattice symmetry to the spin space. Luttinger and Tisza successfully explained several types of magnetic structures by the MDD interaction in their pioneering work [8], and several experimental studies followed [9–11].

The MDD interaction is even more important in geometrically frustrated magnets, where the geometry causes macroscopic degeneracy. For instance, A₂B₂O₇ pyrochlore oxides exhibiting MDD interaction display exotic states which are doubly gauge charged emergent magnetic monopoles [12]. In an artificial magnet, collections of nanomagnetic islands arranged in a kagome lattice generate magnetic moment fragmentation [13]. The combination of the frustrated geometry and the MDD interaction is thus a good playground for a new magnetic state.

In a classical Heisenberg kagome antiferromagnet, the ground state is infinitely degenerated. At zero temperature, the

long-range order of the 120° structures with enlarged $\sqrt{3} \times \sqrt{3}$ unit cells characterized by $\mathbf{k}_{1/3} = (1/3, 1/3, 0)$ in Fig. 1(a) is selected by the order-by-disorder mechanism [14]. The degeneracy of the ground state can be lifted also by various perturbations. The states selected by the Dzyaloshinskii-Moriya (DM) interaction are the 120° structures with $\mathbf{k}_0 = (0, 0, 0)$ [15]; the structures exhibit positive vector chirality in Fig. 1(b) and negative vector chirality in Fig. 1(c). We name DM(+) and DM(–)-type 120° structures for the former and the latter, respectively. The vector chirality is determined by the out-of-plane component of the DM vector. In the DM(+) structure, the easy-axis anisotropy is induced by the in-plane component of the DM vector. The state selected by the MDD interaction is the 120° structure exhibiting *tail-chase* geometry as shown in Fig. 1(d) [16]. It has positive chirality but different easy-axis anisotropy from the DM(+) structure. It is named the MDD-type 120° structure. The structure is equivalent to magnetic vortices on a honeycomb lattice with staggered polarity, which can be a prototype of a natural magnonic crystal [5–7]. The states selected by the second-neighbor interaction are the 120° structure with \mathbf{k}_0 for the antiferromagnetic case and that with $\mathbf{k}_{1/3}$ for the ferromagnetic case [17].

The magnetic structures of the kagome antiferromagnet have been intensively investigated by neutron diffraction on many compounds. The DM(+) structure is realized in most cases, AFe₃(SO₄)₂(OH)₆ (A = K, Na, Ag, Rb, NH₄) [18–21], KCr₃(SO₄)₂(OH)₆ [22], and Nd₃Sb₃Mg₂O₁₄ [23], which may be due to the coincidence between the direction of spins determined by DM interaction and the magnetic easy axis allowed by the crystallographic symmetry. The DM(–) structure is observed in a couple of semimetals Mn₃Sn and Mn₃Ge

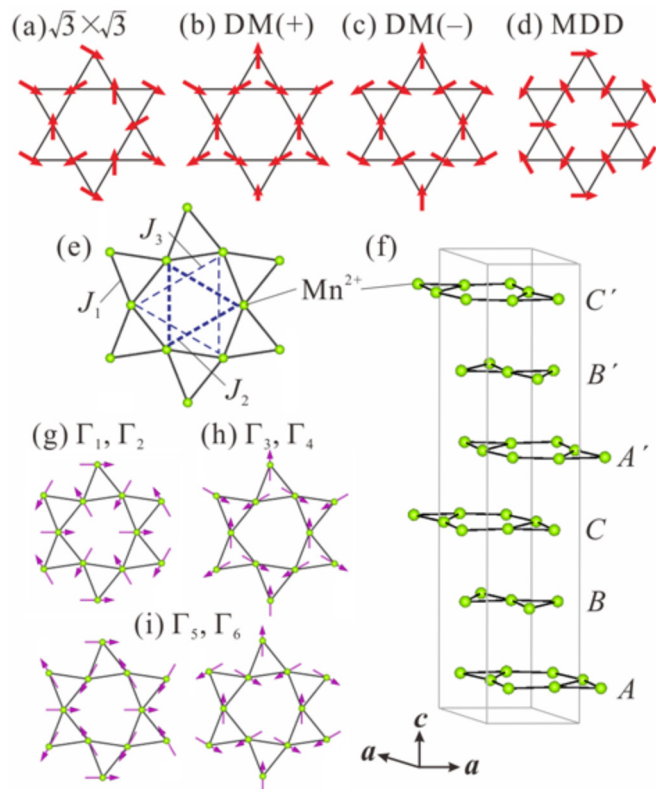


FIG. 1. 120° structures in the kagome lattice. The directions of the spins are represented by the red arrows. (a) 120° structure with the enlarged unit cell by $\sqrt{3} \times \sqrt{3}$. (b) DM(+), (c) DM(-), and (d) MDD-type 120° structure with the propagation vector $\mathbf{k} = 0$. (e) Mn^{2+} ions in a kagome layer in $\text{NaBa}_2\text{Mn}_3\text{F}_{11}$. Solid, thick-dashed, and thin-dashed lines indicate the nearest-, second-, and third-neighbor interactions. The lattice is equivalent to the regular kagome lattice as a spin system (see text). (f) The linear perspective view of the kagome layers. (g)–(i) 120° structures represented by the irreducible representations for $\mathbf{k} = 0$.

exhibiting a large anomalous Hall effect [24]. The $\sqrt{3} \times \sqrt{3}$ structure is found in the high-pressure phase in herbertsmithite $\text{ZnCu}_3(\text{OH})_6\text{Cl}_2$ [25]. The tail-chase structure has been observed in quinary oxalate compounds with Fe^{2+} ion [26,27] so far. Its tail-chase structure was, however, caused by a strong single-ion anisotropy instead of the MDD interaction. To the best of our knowledge, the experimental observation of the tail-chase structure originating from the MDD interaction has not yet been identified (by neutron diffraction), although it is of primary importance to the understanding of the kagome family of compounds.

$\text{NaBa}_2\text{Mn}_3\text{F}_{11}$ crystallizes in a hexagonal structure with the space group $R\bar{3}c$ [28]. Mn^{2+} ions carry spin $S = 5/2$, and MnF_7 pentagonal bipyramids form a kagome lattice in the crystallographic ab plane as shown in Fig. 1(e). The path of the nearest-neighbor interaction J_1 indicated by the solid line is Mn-F-Mn. Although the interior angles of the hexagon in the kagome lattice are shifted from 120° and the lattice is distorted, the length of the sides and the angles of Mn-F-Mn are the same for all the bonds. This means that the magnitudes of the nearest-neighbor interactions are the same. The spin system

is thus regarded as the regular kagome lattice. The six kagome layers are stacked in the unit cell as shown in Fig. 1(f). The A , B , and C layers and the A' , B' , and C' layers are related by the c glide.

The exchange pathways of the second and third-neighbor interaction are unusual; the second-neighbor interaction J_2 indicated by the thick dashed line is Mn-F-Mn, and that of the third-neighbor interaction J_3 indicated by the thin dashed line is Mn-F-F-Mn. The J_3 is thus negligible, and the unique network called the kagome-triangular lattice is realized [29]. The heat capacity and magnetic susceptibility measurements exhibit antiferromagnetic transition at $T_N = 2$ K. The Curie-Weiss temperature θ_{CW} was estimated to be -32 K, which is smaller than those of most kagome lattice magnets [18–23,25]. In addition, the bond angles of the nearest-neighbor exchange pathways are close to 90° rather than 180° [29], suggesting the nearest-neighbor interaction is weak antiferromagnet or ferromagnetic based on the Goodenough-Kanamori rules [30,31]. The exchange interaction in $\text{NaBa}_2\text{Mn}_3\text{F}_{11}$ is thus relatively small, and the MDD interaction may be important.

In this paper, we demonstrate that the tail-chase structure with small incommensurate (IC) modulations is realized in $\text{NaBa}_2\text{Mn}_3\text{F}_{11}$ by using neutron diffraction. Combination of the experiment and calculation suggests that the tail-chase structure selected by the main perturbation of the short-range MDD interaction including up to the fourth neighboring is modulated by a smaller perturbation such as the long-range MDD interaction or the interlayer interaction.

II. EXPERIMENTAL DETAILS

A polycrystalline sample was prepared by a solid state reaction method [29]. The total mass of the obtained sample was 5.4 g. A ^3He cryostat was used to achieve low temperatures. Neutron diffraction experiments were performed using two neutron diffractometers; a powder diffractometer ECHIDNA installed in the OPAL reactor, Australian Nuclear Science and Technology Organization for the preliminary measurement, and the long-wavelength time-of-flight (TOF) diffractometer WISH [32] installed at the ISIS Pulsed Neutron and Muon Source, Rutherford Appleton Laboratory, for the precise measurement. We chose a high-resolution double-frame mode at WISH. The data for the Rietveld refinement in Figs. 2(a) and 2(b) and the temperature dependence of the integrated intensities in Fig. 3(a) were measured by using the detector bank with an average scattering angle of $2\theta = 90^\circ$. The data for the diffuse scattering in Fig. 3(b) were measured by using the detector bank centered at $2\theta = 27^\circ$. The obtained data were analyzed by the Rietveld method using FULLPROF software [33]. Candidates for the magnetic structure compatible with the lattice symmetry were obtained by SARAH software [34].

III. RESULTS AND ANALYSIS

The neutron diffraction profile measured at 20 K is reasonably fitted by the hexagonal structure with the space group $R\bar{3}c$ as shown in Fig. 2(a). The profile factors are $R_{\text{wp}} = 8.80\%$ and $R_e = 4.37\%$, and the obtained parameters are summarized in the cif file in the Supplemental Material [35].

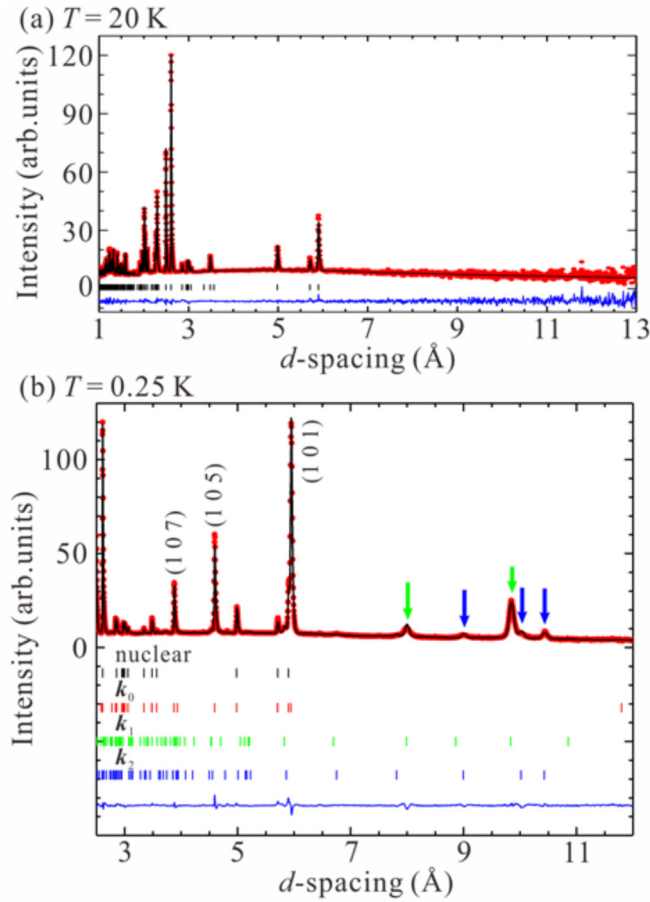


FIG. 2. Neutron diffraction profiles for $\text{NaBa}_2\text{Mn}_3\text{F}_{11}$ at (a) 20 K and (b) 0.25 K. The solid squares and curves show the experimental data and simulations, respectively. The vertical bars show the positions of the nuclear and magnetic Bragg peaks. The solid curves below the bars show the difference between the data and simulations. The green and blue arrows indicate the IC magnetic Bragg peaks with k_1 and k_2 .

At 0.25 K, at least eight additional peaks are observed as shown in Fig. 2(b). The peak intensities increase with the decrease of the temperature below 2.25 K as shown in Fig. 3(a). This means that a magnetic long-range order occurs at $T_N = 2.25$ K, which is consistent with the previous heat capacity measurement [29]. The peaks at $d = 3.8, 4.6,$ and 5.9 \AA are indexed as (1 0 7), (1 0 5), and (1 0 1), meaning that the magnetic propagation vector is $k_0 = (0,0,0)$. The peaks indicated by the green and blue arrows in the long d region are not indexed by the k_0 vector but rather by IC vectors.

Temperature variations of the diffraction profiles are exhibited in Fig. 3(b). At 100 K paramagnetic scattering is observed in the low- Q region. On cooling it is suppressed, and, instead, magnetic diffuse scattering is induced at $Q \sim 1.0 \text{ \AA}^{-1}$ and is more pronounced at 3 K. The diffuse scattering is suppressed with further cooling, and magnetic Bragg peaks appear. The short-range spin correlations thus develop at much higher temperatures than the transition temperature, suggesting the existence of strong geometrical frustration. The behavior is consistent with the heat capacity in which most of the magnetic entropy was released above T_N [29].

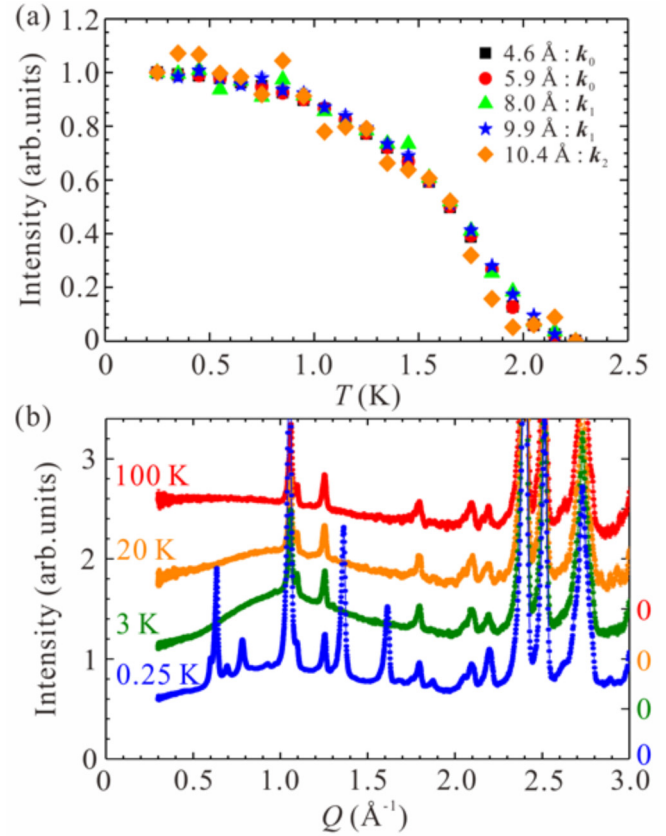


FIG. 3. (a) Temperature evolution of the integrated intensities at $d = 4.6, 5.9, 8.0, 9.9$ and 10.4 \AA . The error bars are inside the markers. Each of the integrated intensities is normalized to their values at 0.25 K and subtracted by their background at 2.25 K. (b) Neutron diffraction profiles at $T = 100, 20, 3,$ and 0.25 K . The profiles are shifted by vertical offsets.

In the magnetic structure analysis, it is assumed that the peaks with k_0 mainly construct the magnetic structure, since the intensities of the peaks with k_0 are larger than those with the IC vectors. The representation analysis [34] with the space group $R\bar{3}c$ and the propagation vector k_0 leads to six irreducible representations (IRs): $\Gamma_1 + \Gamma_2 + \Gamma_3 + \Gamma_4 + 2\Gamma_5 + 2\Gamma_6$. The IRs and the basis vectors are summarized in Table I. The basis vectors for Γ_1 or Γ_2 provide the MDD-type 120° structure in Fig. 1(g), and Γ_3 or Γ_4 provide the DM(+)-type structure in Fig. 1(h), whereas the basis vectors associated with Γ_5 or Γ_6 correspond to the 120° structure with the negative vector chirality as shown in Fig. 1(i). The magnetic structure in the α layer ($\alpha = A, B, C$) and that in the α' layer ($\alpha' = A', B', C'$) are the same for $\Gamma_1, \Gamma_3,$ and Γ_5 . In contrast, the structure in the α' layer is the inverse structure of the α layer for $\Gamma_2, \Gamma_4,$ and Γ_6 . In testing the models of the magnetic structures inferred by the various IRs, it is assumed that the magnitudes of the magnetic moments on the Mn^{2+} ions are all the same. From the Rietveld refinements, we find that only Γ_2 gives a satisfactory agreement with the observed pattern. The refined magnetic structure with k_0 exhibits the 120° structure in the ab plane as shown in Fig. 1(g). The refined magnitude of the moment is $4.14(1) \mu_B$ at 0.25 K, which is 83% of the full moment of the Mn^{2+} ion. According to the J_1 - J_2 phase diagram in the Heisenberg kagome-triangular

TABLE I. Basis vectors for the space group $R\bar{3}c$ with $\mathbf{k} = (0,0,0)$. The atoms of the nonprimitive basis are defined according to Mn1 (0.4438,0,0.25), Mn2 (0,0.4438,0.25), Mn3 (0.5562,0.5562,0.25), Mn4 (0.5562,0,0.75), Mn5 (0,0.5562,0.75), and Mn6 (0.4438,0.4438,0.75).

		Basis vectors [$m_a m_b m_c$]					
IRs		Mn1	Mn2	Mn3	Mn4	Mn5	Mn6
Γ_1	Ψ_1	[2 0 0]	[0 2 0]	[-2 -2 0]	[2 0 0]	[0 2 0]	[-2 -2 0]
Γ_2	Ψ_2	[2 0 0]	[0 2 0]	[-2 -2 0]	[-2 0 0]	[0 -2 0]	[2 2 0]
Γ_3	Ψ_3	[1 2 0]	[-2 -1 0]	[1 -1 0]	[1 2 0]	[-2 -1 0]	[1 -1 0]
	Ψ_4	[0 0 2]	[0 0 2]	[0 0 2]	[0 0 2]	[0 0 2]	[0 0 2]
Γ_4	Ψ_5	[1 2 0]	[-2 -1 0]	[1 -1 0]	[-1 -2 0]	[2 1 0]	[-1 1 0]
	Ψ_6	[0 0 2]	[0 0 2]	[0 0 2]	[0 0 -2]	[0 0 -2]	[0 0 -2]
Γ_5	Ψ_7	[0.5 0 0]	[0 -1 0]	[-0.5 -0.5 0]	[0.5 0 0]	[0 -1 0]	[-0.5 -0.5 0]
	Ψ_8	[0.5 1.5 0]	[0 0.5 0]	[-0.5 1 0]	[0.5 1.5 0]	[0 0.5 0]	[-0.5 1 0]
	Ψ_9	[0 0 1.5]	[0 0 0]	[0 0 -1.5]	[0 0 1.5]	[0 0 0]	[0 0 -1.5]
	Ψ_{10}	$[-\frac{\sqrt{3}}{2} 0 0]$	[0 0 0]	$[-\frac{\sqrt{3}}{2} -\frac{\sqrt{3}}{2} 0]$	$[-\frac{\sqrt{3}}{2} 0 0]$	[0 0 0]	$[-\frac{\sqrt{3}}{2} -\frac{\sqrt{3}}{2} 0]$
	Ψ_{11}	$[\frac{\sqrt{3}}{2} \frac{\sqrt{3}}{2} 0]$	$[\sqrt{3} \frac{\sqrt{3}}{2} 0]$	$[\frac{\sqrt{3}}{2} 0 0]$	$[\frac{\sqrt{3}}{2} \frac{\sqrt{3}}{2} 0]$	$[\sqrt{3} \frac{\sqrt{3}}{2} 0]$	$[\frac{\sqrt{3}}{2} 0 0]$
	Ψ_{12}	$[0 0 \frac{\sqrt{3}}{2}]$	$[0 0 -\sqrt{3}]$	$[0 0 \frac{\sqrt{3}}{2}]$	$[0 0 \frac{\sqrt{3}}{2}]$	$[0 0 -\sqrt{3}]$	$[0 0 \frac{\sqrt{3}}{2}]$
Γ_6	Ψ_{13}	[0.5 0 0]	[0 -1 0]	[-0.5 -0.5 0]	[-0.5 0 0]	[0 1 0]	[0.5 0.5 0]
	Ψ_{14}	[0.5 1.5 0]	[0 0.5 0]	[-0.5 1 0]	[-0.5 -1.5 0]	[0 -0.5 0]	[0.5 -1 0]
	Ψ_{15}	[0 0 1.5]	[0 0 0]	[0 0 -1.5]	[0 0 -1.5]	[0 0 0]	[0 0 1.5]
	Ψ_{16}	$[-\frac{\sqrt{3}}{2} 0 0]$	[0 0 0]	$[-\frac{\sqrt{3}}{2} -\frac{\sqrt{3}}{2} 0]$	$[\frac{\sqrt{3}}{2} 0 0]$	[0 0 0]	$[\frac{\sqrt{3}}{2} \frac{\sqrt{3}}{2} 0]$
	Ψ_{17}	$[\frac{\sqrt{3}}{2} \frac{\sqrt{3}}{2} 0]$	$[\sqrt{3} \frac{\sqrt{3}}{2} 0]$	$[\frac{\sqrt{3}}{2} 0 0]$	$[-\frac{\sqrt{3}}{2} -\frac{\sqrt{3}}{2} 0]$	$[-\sqrt{3} -\frac{\sqrt{3}}{2} 0]$	$[-\frac{\sqrt{3}}{2} 0 0]$
	Ψ_{18}	$[0 0 \frac{\sqrt{3}}{2}]$	$[0 0 -\sqrt{3}]$	$[0 0 \frac{\sqrt{3}}{2}]$	$[0 0 -\frac{\sqrt{3}}{2}]$	$[0 0 \sqrt{3}]$	$[0 0 -\frac{\sqrt{3}}{2}]$

lattice [29], the 120° structure with \mathbf{k}_0 is favored in the case that both J_1 and J_2 are antiferromagnetic. This means that both J_1 and J_2 in this compound are antiferromagnetic in the absence of MDD interaction.

We search the propagation vectors of the IC peaks' corresponding high-symmetry points/lines/planes of the Brillouin zone. The IC peaks are indexed by two propagation vectors: $\mathbf{k}_1 = [0.3209(2), 0.3209(2), 0]$ for the peaks at $d = 8.0$ and 9.9 \AA and $\mathbf{k}_2 = [0.3338(4), 0.3338(4), 0]$ for those at $d = 9.0, 10.0, \text{ and } 10.4 \text{ \AA}$. The IC vectors are close to $\mathbf{k}_{1/3} = (1/3, 1/3, 0)$. The representation analysis with the space group $R\bar{3}c$ and the propagation vectors \mathbf{k}_1 and \mathbf{k}_2 leads to separation of the equivalent Mn sites into the four nonequivalent Mn sites and two IRs, $\Gamma_1 + \Gamma_2$, at each of the four Mn sites. The IRs and the basis vectors are summarized in Table II. We construct the models of the magnetic structure by the linear combinations of the basis vectors in each single IR. The explicit formulas of the magnetic models that are compatible with both propagation vectors and the space group in the case of Γ_2 are as follows:

$$\mathbf{m}_{\text{Mn1a}} = c_4^{(1)}\Psi_4^{(1)} + c_5^{(1)}\Psi_5^{(1)} + c_6^{(1)}\Psi_6^{(1)}, \quad (1)$$

$$\mathbf{m}_{\text{Mn1b}} = c_4^{(1)}\Psi_4^{(1)} + c_5^{(1)}\Psi_5^{(1)} + c_6^{(1)}\Psi_6^{(1)}, \quad (2)$$

$$\mathbf{m}_{\text{Mn2}} = c_2^{(2)}\Psi_2^{(2)} + c_3^{(2)}\Psi_3^{(2)}, \quad (3)$$

$$\mathbf{m}_{\text{Mn3a}} = (c_4^{(1)}\Psi_4^{(3)} + c_5^{(1)}\Psi_5^{(3)}) + c_6^{(1)}\Psi_6^{(3)}, \quad (4)$$

$$\mathbf{m}_{\text{Mn3b}} = (c_4^{(1)}\Psi_4^{(3)} + c_5^{(1)}\Psi_5^{(3)}) + c_6^{(1)}\Psi_6^{(3)}, \quad (5)$$

$$\mathbf{m}_{\text{Mn4}} = c_2^{(2)}\Psi_2^{(4)} + c_3^{(2)}\Psi_3^{(4)}. \quad (6)$$

Here the coordinations of the Mn atoms and the basis vectors $\Psi_i^{(j)}$ are exhibited in Table II. $c_4^{(1)}, c_5^{(1)}, c_6^{(1)}, c_4^{(1)}, c_5^{(1)}, c_6^{(1)}, c_2^{(2)}, c_3^{(2)}$, and $c_3^{(2)}$ are coefficients of the linear combination of the basis vectors. The number of the fitting parameters is 10, which is too many for the number of the observed IC peaks. We therefore assume that the magnetic structures in the six

TABLE II. Basis vectors for the space group $R\bar{3}c$ with $\mathbf{k} = (h, h, 0)$. The atoms of the nonprimitive basis are defined according to Mn1a (0.4438,0,0.25), Mn1b (0,0.4438,0.25), Mn2 (0.5562,0.5562,0.25), Mn3a (0.5562,0,0.75), Mn3b (0,0.5562,0.75), and Mn4 (0.4438,0.4438,0.75).

		Basis vectors [$m_a m_b m_c$]			
IRs		Mn1a	Mn1b	Mn3a	Mn3b
Γ_1	$\Psi_1^{(1)}$	[1 0 0]	[0 1 0]	$\Psi_1^{(3)}$	[1 0 0]
	$\Psi_2^{(1)}$	[0 1 0]	[1 0 0]	$\Psi_2^{(3)}$	[0 1 0]
	$\Psi_3^{(1)}$	[0 0 1]	[0 0 -1]	$\Psi_3^{(3)}$	[0 0 1]
Γ_2	$\Psi_4^{(1)}$	[1 0 0]	[0 -1 0]	$\Psi_4^{(3)}$	[1 0 0]
	$\Psi_5^{(1)}$	[0 1 0]	[-1 0 0]	$\Psi_5^{(3)}$	[0 1 0]
	$\Psi_6^{(1)}$	[0 0 1]	[0 0 1]	$\Psi_6^{(3)}$	[0 0 1]
		Mn2	Mn4		
Γ_1	$\Psi_1^{(2)}$	[1 1 0]	$\Psi_1^{(4)}$	[1 1 0]	
Γ_2	$\Psi_2^{(2)}$	$[\frac{1}{\sqrt{3}} - \frac{1}{\sqrt{3}} 0]$	$\Psi_2^{(4)}$	$[\frac{1}{\sqrt{3}} - \frac{1}{\sqrt{3}} 0]$	
	$\Psi_3^{(2)}$	[0 0 1]	$\Psi_3^{(4)}$	[0 0 1]	

TABLE III. Refined coefficients of the basis vectors for the magnetic models with \mathbf{k}_1 and \mathbf{k}_2 .

\mathbf{k}_1	t_1	t_2	$c_4^{(1)}$	$c_5^{(1)}$	$c_6^{(1)}$	$c_2^{(2)}$	$c_3^{(2)}$
	-1	-1	-2.20(14)	-2.86(34)	-0.63(34)	3.33(34)	-1.34(43)
\mathbf{k}_2	t_1	t_2	$c_4^{(1)}$	$c_5^{(1)}$	$c_6^{(1)}$	$c_2^{(2)}$	$c_3^{(2)}$
	-1	1	0.82(14)	1.76(15)	0.59(24)	-0.23(62)	2.42(20)

layers are as similar as possible, and the formulas used for the refinement are reduced to

$$\mathbf{m}_{\text{Mn1a}} = c_4^{(1)}\Psi_4^{(1)} + c_5^{(1)}\Psi_5^{(1)} + c_6^{(1)}\Psi_6^{(1)}, \quad (7)$$

$$\mathbf{m}_{\text{Mn1b}} = c_4^{(1)}\Psi_4^{(1)} + c_5^{(1)}\Psi_5^{(1)} + c_6^{(1)}\Psi_6^{(1)}, \quad (8)$$

$$\mathbf{m}_{\text{Mn2}} = c_2^{(2)}\Psi_2^{(2)} + c_3^{(2)}\Psi_3^{(2)}, \quad (9)$$

$$\mathbf{m}_{\text{Mn3a}} = t_1(c_4^{(1)}\Psi_4^{(3)} + c_5^{(1)}\Psi_5^{(3)}) + t_2c_6^{(1)}\Psi_6^{(3)}, \quad (10)$$

$$\mathbf{m}_{\text{Mn3b}} = t_1(c_4^{(1)}\Psi_4^{(3)} + c_5^{(1)}\Psi_5^{(3)}) + t_2c_6^{(1)}\Psi_6^{(3)}, \quad (11)$$

$$\mathbf{m}_{\text{Mn4}} = t_1c_2^{(2)}\Psi_2^{(4)} + t_2c_3^{(2)}\Psi_3^{(4)}, \quad (12)$$

where t_1 and t_2 take +1 or -1. This reduces the number of parameters down to 5 and renders the refinement possible. We similarly construct the magnetic models in the case of Γ_1 . The best fit is obtained for Γ_2 , and the parameters are listed in Table III. The profiles at 0.25 K and the fitting results of the model combined with \mathbf{k}_0 , \mathbf{k}_1 , and \mathbf{k}_2 are shown in Fig. 2(b). The R factors for the whole profile are $R_{\text{wp}} = 7.61\%$ and $R_e = 1.02\%$. The magnetic R factors R_{mag} for \mathbf{k}_0 , \mathbf{k}_1 , and \mathbf{k}_2 are 2.71%, 7.62%, and 12.8%. For reference, the best R_{mag} 's for \mathbf{k}_0 are 57% for Γ_1 , 89% for Γ_3 , 80% for Γ_4 , 79% for Γ_5 , and 36% for Γ_6 . The refined magnetic moments in each IC structure with \mathbf{k}_1 and \mathbf{k}_2 form the two-in-one-out (one-in-two-out) structure similar to the kagome spin ice [36]. In addition, they have an out-of-plane component, the directions of which are all up or all down, and the magnitudes of the moments are modulated.

The temperature evolutions of the integrated intensities associated with the propagation vectors \mathbf{k}_0 , \mathbf{k}_1 , and \mathbf{k}_2 are the same as those shown in Fig. 3(a). This suggests that the low-temperature state is a single ordered state, i.e., a multiple- \mathbf{k} state, where the Mn^{2+} moments form a 120° structure in the ab plane, and the IC propagation vectors modulate this 120° structure. The averaged magnitude of the magnetic moment of the Mn^{2+} ion is $4.54 \mu_B$ at 0.25 K, which is 91% of the Mn^{2+} moment ($S = 5/2$).

IV. DISCUSSION

For the calculation of the ground state we assume isotropic Heisenberg interactions, since the orbital angular momentum of the Mn^{2+} ion is zero, at least for the ground state of the isolated Mn^{2+} ion, and the anisotropy and/or asymmetric terms derived from the perturbation of spin-orbit coupling should be small. As described in the Introduction, the geometry of the main framework of $\text{NaBa}_2\text{Mn}_3\text{F}_{11}$ is a kagome-triangular lattice and the MDD interaction is not negligible. The following Hamiltonian in a kagome plane is thus a good approximation

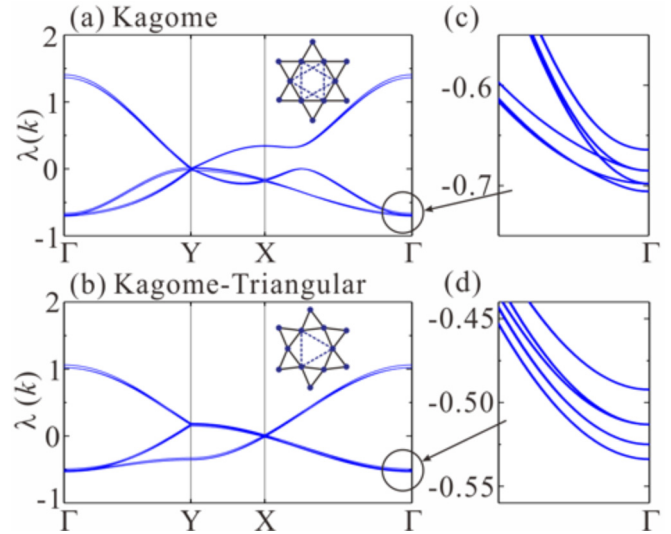


FIG. 4. Eigenvalues of the interaction matrix $J_{ij}^{\alpha\beta}$ along lines in the Brillouin zone. Spectra in (a) the kagome lattice and (b) the kagome-triangular lattice where the exchange interactions are $J_1 = J_2 = 2$ K and the MDD interaction is $J_{\text{MDD}} = 56$ mK. (c) and (d) Detailed structures of the spectra around the Γ point.

for this system:

$$\mathcal{H} = \sum_{\text{n.n.}} J_1 \mathbf{S}_i \cdot \mathbf{S}_j + \sum_{\text{n.n.n.}} J_2 \mathbf{S}_i \cdot \mathbf{S}_j + \sum_{i,j} \frac{\mu_0 (g\mu_B)^2}{4\pi |\mathbf{r}_{ij}|^3} \left[\mathbf{S}_i \cdot \mathbf{S}_j - 3 \frac{(\mathbf{S}_i \cdot \mathbf{r}_{ij})(\mathbf{S}_j \cdot \mathbf{r}_{ij})}{|\mathbf{r}_{ij}|^2} \right], \quad (13)$$

where J_1 and J_2 are the exchange interactions in the nearest- and second-neighbor paths. The third term is the MDD interaction up to the fourth-neighbor path and \mathbf{r}_{ij} is the bond vector between the spins. The strength of the nearest-neighbor MDD interaction J_{MDD} is 56 mK, which is determined from the distance of the nearest-neighbor path $r_{\text{n.n.}}$ as follows:

$$J_{\text{MDD}} \equiv \frac{\mu_0 (g\mu_B)^2}{4\pi r_{\text{n.n.}}^3} = 56 \text{ mK}. \quad (14)$$

In the calculation, the interlayer interaction is not included. To calculate the ground state of the system, we use a Luttinger-Tisza-type theory [8] and investigate the eigenenergies and eigenvectors of the interaction matrix in the wave vector space. The Fourier-transformed Hamiltonian can be written as

$$\mathcal{H} = \sum_{\mathbf{k}} \sum_{i,j} \sum_{\alpha,\beta} J_{ij}^{\alpha\beta}(\mathbf{k}) S_i^\alpha(-\mathbf{k}) S_j^\beta(\mathbf{k}), \quad (15)$$

where $J_{ij}^{\alpha\beta}$ is the sum of J_1 , J_2 , and J_{MDD} . Here, α and β are the Cartesian indices of the spins and i and j run over the three basis sites in the unit cell of the kagome lattice. The spin vector is the Fourier component of the real space, and \mathbf{k} runs over the Brillouin zone of the kagome lattice. Thus, for a given value of \mathbf{k} , $J_{ij}^{\alpha\beta}$ is a 9×9 matrix that needs to be diagonalized. We calculate the following two cases: the kagome lattice with second-neighbor interaction in Fig. 4(a) and the kagome-triangular lattice in Fig. 4(b). The $(0,0,0)$, $(1/3,1/3,0)$, and $(1/2,0,0)$ points of the Brillouin zone are

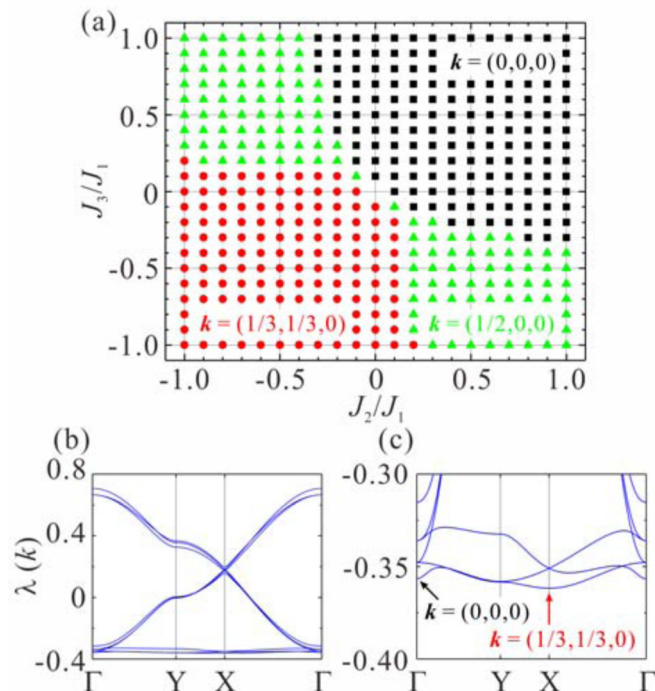


FIG. 5. (a) Phase diagram of the kagome-triangular antiferromagnet having J_3 interaction. MDD interaction is not included. (b) and (c) Eigenvalues of the interaction matrix $J_{ij}^{\alpha\beta}$ for the kagome-triangular antiferromagnet having J_3 and the MDD interaction along lines in the Brillouin zone, where the parameters are $J_1 = 2K$ and $J_2 = J_3 = -J_{\text{MDD}}/2$. Panel (b) is for the wide energy range and the panel (c) is for the low-energy range. A double-minima structure is observed.

labeled as Γ , X , and Y , respectively. In order to realize the 120° structure with $\mathbf{k} = 0$, we set antiferromagnetic interactions for both J_1 and J_2 [17,29]. Since varying J_2/J_1 does not make a significant difference to the results within a wide range of values, the exchange interactions are parametrized at $J_1 = J_2$ for simplicity. We also put $J_1 > J_{\text{MDD}}$ because the Curie-Weiss temperature $\theta_{\text{CW}} = -32\text{ K}$ [29] is larger than the $J_{\text{MDD}} = 56\text{ mK}$.

The eigenenergy $\lambda(\mathbf{k})$ is minimized for $\mathbf{k} = 0$ in both lattices as shown in Figs. 4(a) and 4(b), which implies that the MDD-type 120° structure in Fig. 1(d) is realized for both kagome and kagome-triangular lattices. This result is consistent with the previous study [16]. Although the six states are degenerated at $\mathbf{k} = 0$ in the absence of MDD interaction, the degeneracy is lifted by the interaction as shown in Figs. 4(c) and 4(d). The calculated ground states correspond to the magnetic structure having \mathbf{k}_0 in the experiment, but they do not reproduce the multiple- \mathbf{k} structure.

For the multiple- \mathbf{k} structure, we calculated the ground state of the kagome-triangular antiferromagnet including J_3 interaction in Fig. 1(e). The obtained phase diagram of $J_3/J_1 - J_2/J_1$, where J_1 is antiferromagnetic, is shown in Fig. 5(a). We have presumed that $J_1 \sim J_2 \gg |J_3|$ so far, and the observed \mathbf{k}_0 structure is confirmed by the calculation in this region. In case that J_2 and J_3 are ferromagnetic, i.e., in the third

quadrant, the state of $\mathbf{k}_{1/3} = (1/3, 1/3, 0)$ which is close to the experimentally observed IC vectors \mathbf{k}_1 and \mathbf{k}_2 appears. The ground energy has, however, a single minimum in the \mathbf{k} space, and the observed a multiple- \mathbf{k} structure cannot be explained. Then the MDD interaction up to the 4th-neighbor paths is included, and the eigenvalues of the interaction matrix for $J_1 = 2K$, $J_2 = J_3 = -J_{\text{MDD}}/2$ is obtained as shown in Figs. 5(b) and 5(c). Local minima appear at $\mathbf{k} = (1/3, 1/3, 0)$ and $(0, 0, 0)$, indicating the multiple- \mathbf{k} structure. We found that the MDD interaction mixes the \mathbf{k}_0 structure in the first quadrant and $\mathbf{k}_{1/3}$ structure in the third quadrant in the $J_3/J_1 - J_2/J_1$ phase diagram. The spin structure for \mathbf{k}_0 is the tail-chase structure which is consistent with the experiment. The one for $\mathbf{k}_{1/3}$ has solely out-of-plane component, and it exhibits up-up-down structure. This is inconsistent with the experimentally obtained structure. We have surveyed a series of parameters and exact match to the experimental structure could not be found. Thus, the terms in Eq. (13) do not explain the observed multiple- \mathbf{k} structure, and neither does J_3 . Detailed theoretical studies considering further interactions including the long-range MDD interaction and/or the interlayer interaction are necessary to reproduce the observed multiple- \mathbf{k} structure including IC modulation for the future work.

The reason why the MDD interaction is the main perturbation in $\text{NaBa}_2\text{Mn}_3\text{F}_{11}$ is due to the fact that the exchange interaction is weak compared with most of kagome antiferromagnets having O^{2-} as anion that transfers the exchange integral [18–23]. Hybridization of the d and p orbitals is small in fluorides compared with oxides since covalency of F^- ion is weaker than that of O^{2-} ion. In addition, the edge-sharing of the pentagonal bipyramids MnF_7 in the nearest neighbor path weakens the antiferromagnetic exchange interaction. The superexchange interaction is thus weak and, consequently, the DM interaction, which is the resulting term of the perturbative treatment of the exchange interaction and spin-orbit interaction in the Heisenberg spin Hamiltonian, is also weak. Furthermore, the charge distribution of the Mn^{2+} ion is spherical and prevents the appearance of single-ion anisotropy, since the $3d$ orbitals are half filled, with five electrons coupled, giving rise to an angular momentum $L = 0$. The MDD interaction hence causes the main perturbation in $\text{NaBa}_2\text{Mn}_3\text{F}_{11}$.

V. CONCLUSION

In conclusion the MDD-type 120° structure with an IC modulation was identified in $\text{NaBa}_2\text{Mn}_3\text{F}_{11}$ by the combination of the neutron diffraction measurement and magnetic structure analysis. Classical calculations showed that the MDD interaction is the main perturbative term for the selection of the magnetic ground state. To elucidate the precise IC structure and to identify its origin, further investigations, for instance, single crystal neutron diffraction, are required. Theoretical calculation including long-range MDD interactions may elucidate the IC structure, as was the case with the field-induced IC structure in the gadolinium gallium garnet [37,38]. Consideration of the interlayer interaction would also be important. In addition, the study of magnetic dynamics would be beneficial for the search for exotic states induced by the MDD interaction.

ACKNOWLEDGMENTS

We are grateful to G. J. Nilsen and R. Okuma for helpful discussion. Travel expenses for the neutron diffraction experiments performed using ECHIDNA at ANSTO, Australia, and WISH at ISIS, United Kingdom, were supported by the General User Program for Neutron Scattering Experiments, Institute for Solid State Physics, The University of Tokyo (Proposal No. 13559 and No. 00499), at JRR-3, Japan Atomic

Energy Agency, Tokai, Japan. S.H. was supported by the Japan Society for the Promotion of Science through the Leading Graduate Schools (MERIT). This work was partially supported by KAKENHI (Grant No. 15K17701). T.O. was supported by the Ministry of Education, Culture, Sports, Science and Technology (MEXT) of Japan as a social and scientific priority issue (creation of new functional devices and high-performance materials to support next-generation industries; CDMSI) to be tackled by using the post-K computer.

-
- [1] J. Stuhler, A. Griesmaier, T. Koch, M. Fattori, T. Pfau, S. Giovanazzi, P. Pedri, and L. Santos, *Phys. Rev. Lett.* **95**, 150406 (2005).
- [2] H. M. Rønnow, R. Parthasarathy, J. Jensen, G. Aeppli, T. F. Rosenbaum, and D. F. McMorrow, *Science* **308**, 389 (2005).
- [3] C. Kraemer, N. Nikseresht, J. O. Piatak, N. Tsyrlin, B. D. Piazza, K. Kiefer, B. Klemke, T. F. Rosenbaum, G. Aeppli, C. Gannarelli, K. Prokes, A. Podlesnyak, T. Strässle, L. Keller, O. Zaharko, K. W. Krämer, and H. M. Rønnow, *Science* **336**, 1416 (2012).
- [4] E. Burzuri, F. Luis, B. Barbara, R. Ballou, E. Ressouche, O. Montero, J. Campo, and S. Maegawa, *Phys. Rev. Lett.* **107**, 097203 (2011).
- [5] S. Sugimoto, Y. Fukuma, S. Kasai, T. Kimura, A. Barman, and Y. C. Otani, *Phys. Rev. Lett.* **106**, 197203 (2011).
- [6] S. Jain, V. Novosad, F. Y. Fradin, J. E. Pearson, V. Tiberkevich, A. N. Slavin, and S. D. Bader, *Nat. Commun.* **3**, 1330 (2012).
- [7] M. Hänze, C. F. Adolff, B. Schulte, J. Möller, M. Weigand, and G. Meier, *Sci. Rep.* **6**, 22402 (2016).
- [8] J. M. Luttinger and L. Tisza, *Phys. Rev.* **70**, 954 (1946).
- [9] W. L. Roth, *Phys. Rev.* **110**, 1333 (1958).
- [10] A. Schrön, C. Rödl, and F. Bechstedt, *Phys. Rev. B* **86**, 115134 (2012).
- [11] D. C. Johnston, *Phys. Rev. B* **93**, 014421 (2016).
- [12] J. S. Gardner, M. J. P. Gingras, and J. E. Greedan, *Rev. Mod. Phys.* **82**, 53 (2010).
- [13] C. Nisoli, R. Moessner, and P. Schiffer, *Rev. Mod. Phys.* **85**, 1473 (2013).
- [14] J. N. Reimers and A. J. Berlinsky, *Phys. Rev. B* **48**, 9539 (1993).
- [15] M. Elhajal, B. Canals, and C. Lacroix, *Phys. Rev. B* **66**, 014422 (2002).
- [16] M. Maksymenko, V. R. Chandra, and R. Moessner, *Phys. Rev. B* **91**, 184407 (2015).
- [17] J.-C. Domenge, P. Sindzingre, C. Lhuillier, and L. Pierre, *Phys. Rev. B* **72**, 024433 (2005).
- [18] T. Inami, M. Nishiyama, S. Maegawa, and Y. Oka, *Phys. Rev. B* **61**, 12181 (2000).
- [19] A. S. Wills, *Phys. Rev. B* **63**, 064430 (2001).
- [20] A. S. Wills, A. Harrison, C. Ritter, and R. I. Smith, *Phys. Rev. B* **61**, 6156 (2000).
- [21] D. Grohol, D. G. Nocera, and D. Papoutsakis, *Phys. Rev. B* **67**, 064401 (2003).
- [22] T. Inami, T. Morimoto, M. Nishiyama, S. Maegawa, Y. Oka, and H. Okumura, *Phys. Rev. B* **64**, 054421 (2001).
- [23] A. Scheie, M. Sanders, J. Krizan, Y. Qiu, R. J. Cava, and C. Broholm, *Phys. Rev. B* **93**, 180407(R) (2016).
- [24] T. Nagamiya, S. Tomiyoshi, and Y. Yamaguchi, *Solid State Commun.* **42**, 385 (1982).
- [25] D. P. Kozlenko, A. F. Kusmartseva, E. V. Lukin, D. A. Keen, W. G. Marshall, M. A. de Vries, and K. V. Kamenev, *Phys. Rev. Lett.* **108**, 187207 (2012).
- [26] E. Lhotel, V. Simonet, J. Ortloff, B. Canals, C. Paulsen, E. Suard, T. Hansen, D. J. Price, P. T. Wood, A. K. Powell, and R. Ballou, *Phys. Rev. Lett.* **107**, 257205 (2011).
- [27] E. Lhotel, V. Simonet, J. Ortloff, B. Canals, C. Paulsen, E. Suard, T. Hansen, D. J. Price, P. T. Wood, A. K. Powell, and R. Ballou, *Eur. Phys. J. B* **86**, 248 (2013).
- [28] J. Darriet, M. Ducau, M. Feist, A. Tressaud, and P. Hagemuller, *J. Solid State Chem.* **98**, 379 (1992).
- [29] H. Ishikawa, T. Okubo, Y. Okamoto, and Z. Hiroi, *J. Phys. Soc. Jpn.* **83**, 043703 (2014).
- [30] J. B. Goodenough, *Phys. Rev.* **100**, 564 (1955).
- [31] J. Kanamori, *J. Phys. Chem. Solids* **10**, 87 (1959).
- [32] L. C. Chapon, P. Manuel, P. G. Radaelli, C. Benson, L. Perrott, A. Ansell, N. J. Rhodes, D. Raspino, D. Duxbury, E. Spill, and J. Norris, *Neutron News* **22**, 22 (2011).
- [33] J. Rodriguez-Carvajal, *Phys. B (Amsterdam, Neth.)* **192**, 55 (1993).
- [34] A. S. Wills, *Phys. B (Amsterdam, Neth.)* **276**, 680 (2000).
- [35] See Supplemental Material at <http://link.aps.org/supplemental/10.1103/PhysRevB.97.054411> for a summary of the structural parameters.
- [36] A. S. Wills, R. Ballou, and C. Lacroix, *Phys. Rev. B* **66**, 144407 (2002).
- [37] T. Yavors'kii, M. Enjalran, and M. J. P. Gingras, *Phys. Rev. Lett.* **97**, 267203 (2006).
- [38] N. d'Ambrumenil, O. A. Petrenko, H. Mutka, and P. P. Deen, *Phys. Rev. Lett.* **114**, 227203 (2015).